

# Cobalt oxide (Co<sub>3</sub>O<sub>4</sub>)/graphene nanosheets (GNS) composite prepared by novel route for supercapacitor application

A. Nirmalesh Naveen<sup>1</sup> · P. Manimaran<sup>1</sup> · S. Selladurai<sup>1</sup>

Received: 5 May 2015 / Accepted: 2 August 2015 / Published online: 6 August 2015  
© Springer Science+Business Media New York 2015

**Abstract** Cobalt oxide (Co<sub>3</sub>O<sub>4</sub>)-graphene nanosheets (GNS) composite was prepared using a novel route. Room temperature prepared graphite oxide was exfoliated at low temperature and subsequently reduced to GNS by chemical method. Successful compound formation was confirmed and structural details were obtained from XRD studies. Cobalt oxide was found to crystallize in spinel fcc structure with average crystallite size of 9 nm in the composite. FTIR and XPS study confirms the removal of oxygen containing functional group in reduced graphene and spinel formation of cobalt oxide in the composite. Raman spectra depict the reestablishment of sp<sup>2</sup> conjugated network of carbon atoms, on reduction to graphene. FESEM images reveal the nanosheet like morphology of the graphene being retained in the composite and promoting ion diffusion channels. Electrochemical characterization discloses the pseudocapacitive behaviour of the composite material. Higher specific capacitance of 650 F/g was exhibited by GNS-Co<sub>3</sub>O<sub>4</sub> at 5 mV/s scan rate. Symmetrical supercapacitor fabricated using GNS-Co<sub>3</sub>O<sub>4</sub> demonstrated superior power characteristics. Graphene in the composite has substantially increased the electron and ion transport in the electrode material leading to enhanced performance.

## 1 Introduction

Everyday energy requirement and demand is in increasing pace across the world. Researchers are putting more effort into efficient way of energy production,

storage and transport. Capacitors are devices used to store electrical energy by electrostatic charge separation. Energy storage has been revolutionized after the introduction of electrochemical capacitors or supercapacitors. Owing to their high power density, long cycle life, short charging time, good safety, and so forth [1–5]. They possess higher energy density compared to conventional capacitors and high power density than batteries. Therefore they are either directly used as power source or auxiliary power source along with batteries. Also, they are suitable for harvesting transient energy from renewable resources like wind, solar, tide etc. [6, 7]. Capacitor's capacitance solely depends on the properties of electrode material used. Hence, by tailoring the properties of electrode material the capacitance can be enhanced substantially. Materials for supercapacitors can be broadly categorized into two types based on their charge storage mechanism (1) Carbon based materials (Graphene, CNT, MWCNT, SWCNT etc.) exhibiting electric double layer capacitance originating from electrostatic separation of charges at the electrode-electrolyte interface; (2) metal oxides (Co<sub>3</sub>O<sub>4</sub>, NiO, Fe<sub>2</sub>O<sub>3</sub>, MnO<sub>2</sub>, RuO<sub>2</sub> etc.) and conducting polymers (PANI, PVP, PEDOT, PPY etc.) that exhibit pseudocapacitance by the faradaic redox process occurring within the bulk of the material [8–12]. Ruthenium oxide (RuO<sub>2</sub>) exhibits ideal capacitive behaviour, but its applicability was hindered by high cost and toxicity which made the search for alternating high performance electrode material inevitable [13, 14]. Among the transition metal oxides, cobalt oxide (Co<sub>3</sub>O<sub>4</sub>) that crystallizes in the cubic spinel structure shows better electro-activeness than any other material. Previous studies suggest that compared to individual materials, composites of metal oxide have shown enhanced capacitive behavior [15].

✉ A. Nirmalesh Naveen  
nirmalesh.naveen@gmail.com

<sup>1</sup> Ionics Lab, Department of Physics, Anna University, Chennai, Tamil Nadu 600025, India

Graphene is a two dimensional arrangement of one atom thick  $sp^2$  carbon atoms. Unique structure and arrangement have made graphene popular among the researchers which are evident from the number of research papers published recently. Owing to its remarkable electrical properties, unusual mechanical properties and ultra-large specific surface area, graphene has gained wide applications in field-effect transistors, transparent conducting films, lithium ion batteries, supercapacitors and ultra-sensitive sensors [16–18]. There are two approaches for the synthesis of graphene (1) top down approach and (2) bottom up approach. In both cases, natural graphite (which is a stacked sheet of graphene) is used as the starting material for the preparation of graphene. Top down approach involves mechanical peeling of graphene layer by layer from graphite using scotch tape or high power ultrasonication which is always tedious and gives low yield. Widely, graphene is synthesized by oxidation of graphite to graphite oxide (GO) in the presence of concentrated acids using methods developed by Hummers, Brodie and Staudenmeier. Graphite can be assumed to be a stacked graphene sheet with interplanar spacing of 0.34 nm held together by weak van der Waals force. Introduction of oxygen containing functional groups through oxidation increases the d spacing with obvious decrease in the binding energy. Ultrasonication at high power or thermal energy is sufficient to separate and obtain individual sheets of graphene oxide [19]. Since  $\pi$  electrons are consumed by the functional groups, GO acts as an insulator. Reduction (removal of oxygen containing functional groups) of graphene oxide restores the electrical conductivity of graphene close to the level of graphite. Thermal exfoliation of graphene proceeds by vaporization of intercalated water molecules and other carboxyl groups producing  $H_2O$ ,  $CO_2$  and  $CO$  gases which increase the interplanar pressure leading to exfoliation. In general, exfoliation and simultaneous reduction of graphene occurs at elevated temperature in the range of 1050 °C [20]. Recently, there are reports on vacuum assisted low temperature thermal exfoliation and hydrogen induced low temperature exfoliation of graphene, involving more time and complexity [21].

Here, we have developed a simple method for low temperature (150 °C) thermal exfoliation of graphene oxide and subsequent reduction using chemical method. Further cobalt oxide–graphene ( $Co_3O_4$ –GNS) composite was prepared to evaluate the impact of graphene on the electrochemical performance of composite material and is compared with pristine cobalt oxide ( $Co_3O_4$ ). Structural and chemical properties that have notable influence on the

material's performance were studied using suitable characterization techniques and their results are discussed below.

## 2 Experimental

Graphite nanoparticles, cobaltous nitrate and  $KMnO_4$  were purchased from Alfa Aesar. Urea, conc. sulfuric acid ( $H_2SO_4$ ), orthophosphoric acid ( $H_3PO_4$ ), hydrochloric acid (HCl) and hydrogen peroxide (30 %) were of analytical grade and used as purchased.

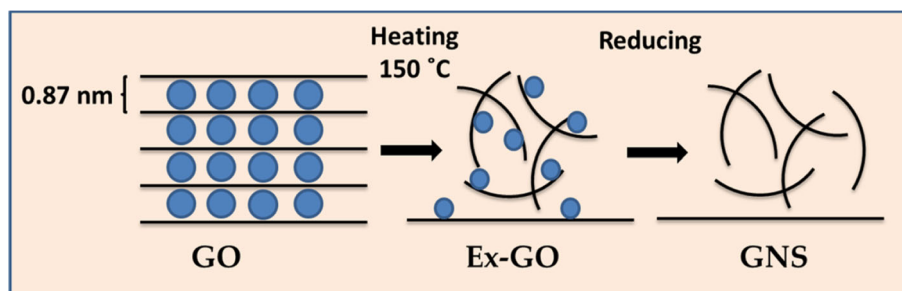
### 2.1 Preparation of graphite oxide (GO)

Novel room temperature synthesis of graphite oxide involves slight modification in the improved Hummer's method. In this typical synthesis procedure, 1.6 g of graphite powder was added to the mixture of 160 mL  $H_2SO_4$  and 40 mL orthophosphoric acid (4: 1 ratio) under stirring. To the vigorously agitated solution, 9 g of  $KMnO_4$  (oxidant) was added in small portions with 10 min time interval. Above mixture was left for 3 days under stirring for complete oxidation of graphite. Gas evolution from the reactants ceases at the end of 3 days. Further,  $H_2O_2$  was added to the solution which reacts exothermically turning the dark reactant solution into brilliant yellow colour indicating the complete oxidation of graphite oxide. Obtained yellow solution was washed repeatedly with copious amount of warm water and 1 M HCl solution. Washing with HCl solution was necessary to remove the sulfate ions from the product. Brown coloured hydrophilic GO was separated by centrifuging the solution at high rpm and dried in vacuum at 80 °C for 24 h. High yield of 82 % GO was obtained from this synthesis method.

### 2.2 Low temperature thermal exfoliation of GO

Obtained GO was introduced into a muffle furnace preheated at 150 °C. Within 5 min complete exfoliation of GO occurred. Volume of exfoliated graphite oxide (Ex-GO) was 100 times higher than the volume of actual GO placed. Graphical representation of graphene nanosheets preparation is shown in Scheme 1. Advantage of pre-exfoliation before reduction is that the reducing agents will have better access to the graphite oxide reactive sites. By this method reduction percentage can be increased substantially and produces good quality graphene sheets.

**Scheme 1** Graphical representation of GNS preparation



### 2.3 Ex-GO reduction and GNS–Co<sub>3</sub>O<sub>4</sub> composite preparation

To prepare GNS–Co<sub>3</sub>O<sub>4</sub> composite, 50 mg of Ex-GO was dispersed in 100 mL of water. To the above solution 10 mM of cobaltous nitrate (Co(NO<sub>3</sub>)<sub>2</sub>·6H<sub>2</sub>O) was added in drops under stirring. Subsequently 12 mM of urea was added to the mixture (to promote hydrolysis) and the solution was transferred to a 250 mL round bottom flask for heating at 120 °C under refluxing for 6 h. Pink-black precipitate formed was separated using centrifuge and washed repeatedly with water and ethanol. Resultant powder was calcined in air at 400 °C for 3 h to obtain GNS–Co<sub>3</sub>O<sub>4</sub> composite.

To prepare pristine cobalt oxide and GNS separately, similar procedure was followed. For GNS preparation cobaltous nitrate was excluded and for cobalt oxide preparation Ex-GO was excluded. Pink precipitate obtained in the case of cobalt oxide was washed repeatedly and calcined at 400 °C for 3 h in air. Black hydrophobic precipitate obtained for GNS was washed, filtered and heated at 150 °C for 3 h in nitrogen gas flow.

### 2.4 Materials characterization

X-ray diffractogram of the samples were recorded by Bruker X-ray diffractometer D2 PHASER model. K $\alpha$  radiation of copper target with a wavelength of 1.5416 Å was used as X-ray source. Detected diffraction angle ( $2\theta$ ) was scanned from 10° to 80° with a step size of 0.02°. Fourier Transformed Infrared (FTIR) spectra of the samples were recorded between 500–4000 cm<sup>-1</sup> wavenumber using FTIR spectrophotometer (Bruker). Raman spectra were recorded from Horiba Jobin–Yvon LabRAM HR 800 Dual Microscope LASER RAMAN using Ar-Ion gas laser with emission at 488 nm. Morphology of the samples was imaged using FEI Quanta FEG 200—Field Emission Scanning Electron Microscope (FESEM). X-ray photoelectron spectra were recorded using Kratos AXIS Ultra DLD X-ray Photoelectron Spectrometer (XPS) with aluminium anode (monochromatic K $\alpha$  X-rays 1.486 eV of energy) as source and operating at 160 eV pass energy. All

binding energy values were charge-corrected to the C 1s signal which was set at 284.6 eV. XPS spectra were analyzed and fitted using CasaXPS software (version 2.3.16).

### 2.5 Electrochemical characterization

Prepared electrode material, activated carbon and polyvinylidene fluoride (PVDF) binder were mixed together in the ratio of 85:5:10 (wt%). A slurry of the mixture was made using *N*-Methyl-2-pyrrolidone (NMP), which was coated onto a nickel foil current collector of (1 × 1 cm) 0.5 mm thickness (produced by Alfa Aesar) and dried for 4 h to remove the solvent. The mass of the loaded samples lies within the range of 0.4–0.5 mg measured using a Shimadzu analytical balance of accuracy 0.01 mg. Cyclic Voltammetry (CV), Chronopotentiometry (CP) and Electrochemical Impedance studies (EIS) were performed using a CHI 661C electrochemical workstation employing a standard 3-electrode cell configuration with platinum wire as counter electrode and Standard Calomel Electrode (SCE) as a reference electrode. The measurements were performed using aqueous 1 M KOH electrolyte at ambient conditions.

### 2.6 Fabrication of symmetrical capacitor

For the fabrication of symmetrical capacitor, GNS–Co<sub>3</sub>O<sub>4</sub> electrode material, activated carbon and polyvinylidene fluoride (PVDF) binder were mixed together in the ratio of 85:5:10 (wt%). A slurry of the mixture was made using *N*-Methyl-2-Pyrrolidone (NMP), which was coated onto a nickel foil current collector of (1 × 1 cm) 0.25 mm thickness (produced by Alfa Aesar) and dried for 4 h at 80 °C to remove the solvent. Two identical electrodes were prepared with mass loading of 0.5 mg each. PTFE membrane of pore size 0.4 μm was used as the separator. Prior to fabrication membrane was soaked into 3 M KOH electrolyte solution for impregnation. Later, membrane was sandwiched between the electrodes. Cell was held together by insulated clips and electrical contacts were drawn from the cell. Schematic illustration of symmetrical capacitor fabrication is provided in Scheme 2.

### 3 Results and discussion

#### 3.1 XRD studies

The phase identity and structural information of the prepared nano-crystalline powders were obtained from Powder X-ray Diffraction (PXRD) pattern. Figure 1a contains the XRD patterns of graphite oxide (GO), exfoliated graphite oxide (Ex-GO) and reduced graphene nanosheets (GNS). Inset of the figure shows the digital photograph of sample container with GO before exfoliation and after exfoliation at 150 °C. For graphite oxide the diffraction peaks appear at around  $2\theta = 10^\circ$  and  $42^\circ$ , corresponding to

the (001) and (100) reflection of GO, the interlayer spacing calculated from the Bragg's equation was 0.87 nm [22, 23]. Due to the introduction of various functional groups like hydroxyl, epoxy and carboxyl groups in graphite lattice, (002) peak (at  $2\theta = 26.3^\circ$ ) of pristine graphite shifts to lower angle at  $2\theta = 10.08^\circ$  accompanied with an increase in the d spacing [24]. Exfoliation of graphite at 150 °C was reflected in the XRD pattern by the occurrence of peak broadening and shifting in peak position to  $11.48^\circ$ . Water molecules and other volatile materials present within the lattice of graphite oxide on heating decomposes violently resulting in exfoliation of GO and lattice spacing decreases to 0.77 nm. After chemical reduction to GNS

**Scheme 2** Schematic illustration of GNS–Co<sub>3</sub>O<sub>4</sub> based symmetrical capacitor fabrication

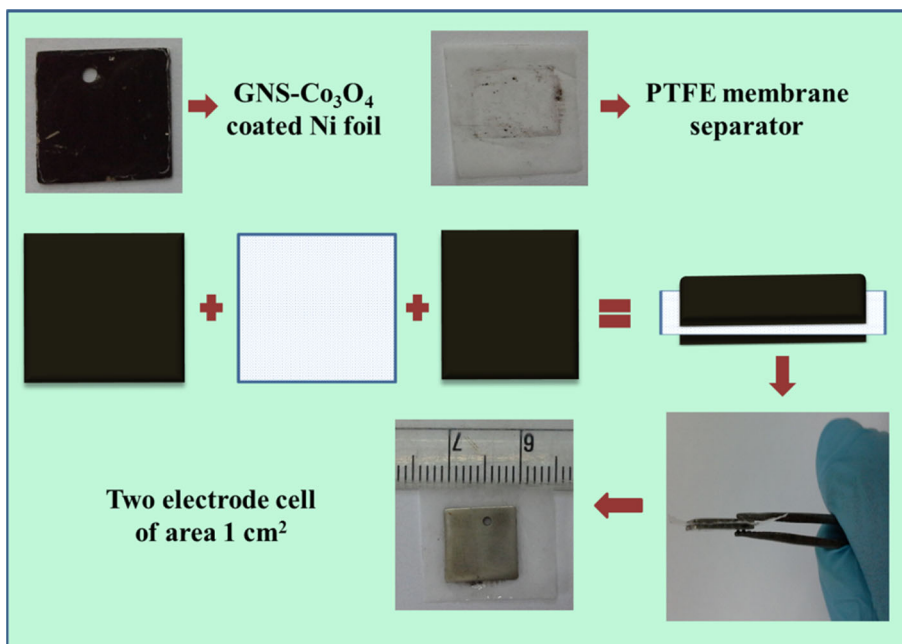
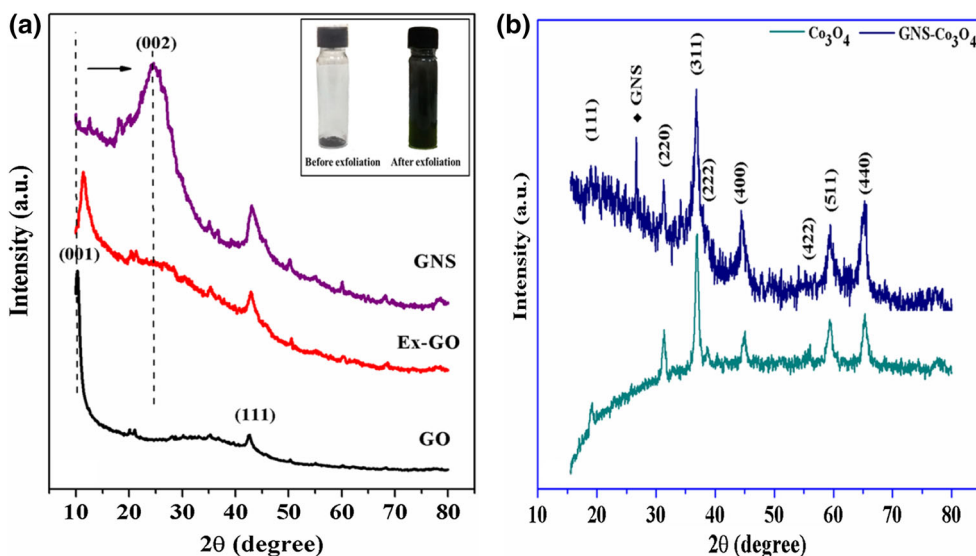


**Fig. 1** The powder X-ray diffraction (PXRD) pattern of **a** GO, Ex-GO and GNS and **b** Co<sub>3</sub>O<sub>4</sub> and GNS–Co<sub>3</sub>O<sub>4</sub>



most of the oxygen-containing functional groups were removed which causes the graphene peak to shift to  $2\theta = 24.59^\circ$  and decrease in lattice spacing to 0.36 nm [25]. This suggests that the conjugated graphene network ( $sp^2$  carbon) was reestablished during the reduction process. Figure 1b exhibits the XRD pattern of pristine spinel cobalt oxide and graphene–cobalt oxide composite material. For pristine cobalt oxide eight diffraction peaks corresponding to (111), (220), (311), (222), (400), (422), (511) and (440) planes were indexed to face centered cubic phase of  $Co_3O_4$  crystalline structure with space group  $FD-3m$  [Joint Committee on Powder Diffraction Standards (JCPDS) file no. 78-1970] [26]. Absence of secondary peaks other than those expected for cobalt oxide denotes the structural and phase purity of the compound. For composite material, apart from the diffraction peaks observed for  $Co_3O_4$  it also contains an additional peak at  $2\theta = 25.5^\circ$  corresponding to GNS. Crystallinity of cobalt oxide decreases with the introduction of graphene in the composite. Average crystallite size of the particles were calculated for the samples using Scherrer formula given below

$$d = \frac{0.9 \times \lambda}{\beta \cos\theta} \quad (1)$$

$d$  is the crystallite size,  $\lambda$  is the X-ray wavelength (1.542 Å),  $\theta$  is the Bragg diffraction angle and  $\beta$  is the full width at the half maximum (FWHM) of the diffraction peak [27]. Crystallite size of 13 nm calculated for pristine cobalt oxide decreases to 9 nm in the composite. Graphene introduction has resulted in the reduction of average crystallite size.

### 3.2 FTIR studies

Fourier Transformed Infrared (FTIR) spectra recorded for the samples between 500 and 4000  $cm^{-1}$  wavenumber is displayed in Fig. 2. GO spectrum reveals the presence of various oxygen containing functional groups attached to the graphite lattice on oxidation. Band at 3417 and 1628  $cm^{-1}$  was attributed to the stretching vibrations and deformation vibrations of hydroxyl groups, respectively [28]. C=O stretching vibration of  $sp^2$  carbon belonging to carboxyl COOH groups situated at the edges of graphite oxide sheets was observed at 1729  $cm^{-1}$ . Appearance of a peak at 1329  $cm^{-1}$  was may be due to the presence of tertiary C–OH groups [29]. Stretching vibrations of epoxy (C–O) were observed at 1090  $cm^{-1}$  and asymmetric stretching vibrations at 802  $cm^{-1}$  [30]. Peaks corresponding to oxygen-containing functional groups were suppressed in the reduced graphene sheets which confirms the successful reduction of GO. Lower part of the figure exhibits the FTIR spectra recorded for cobalt oxide and

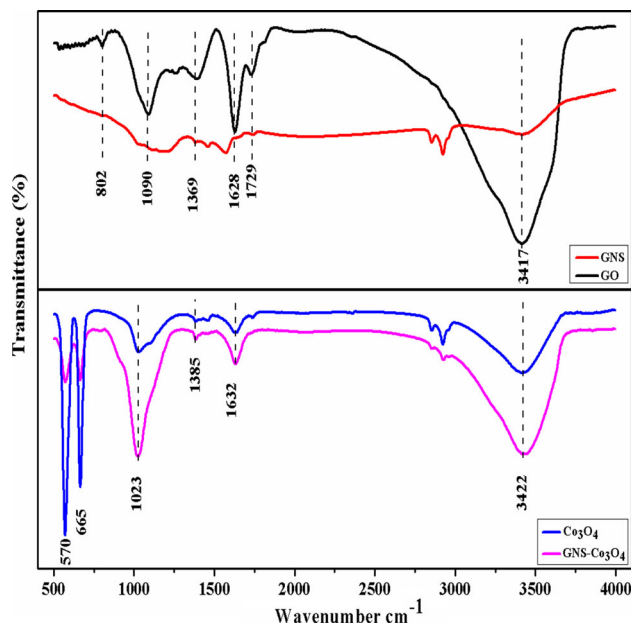


**Fig. 2** FTIR spectra of GO, GNS,  $Co_3O_4$  and GNS– $Co_3O_4$  recorded between 500 and 4000  $cm^{-1}$

GNS– $Co_3O_4$ . The IR spectra of  $Co_3O_4$  display two very strong peaks at 570 and 665  $cm^{-1}$ . Observed peaks were characteristics of  $OB_3$  (B— $Co^{3+}$  in an octahedral site) and  $ABO$  (A— $Co^{2+}$  in the tetrahedral site) vibrations in the  $Co_3O_4$  spinel lattice respectively [26]. Characteristic peaks of  $Co_3O_4$  were also present in the FTIR spectrum of composite. This further confirms the formation of spinel cobalt oxide in pristine form and in the graphene composite. Above results are in good agreement with the XRD studies. Increased intensity of peak at 1023  $cm^{-1}$  in the GNS– $Co_3O_4$  system corresponding to C–O stretching vibrations was due to the intake of oxygen during calcination at 400 °C in air.

### 3.3 Raman studies

Raman study is considered as the most vital technique for characterization of graphene and related materials. Figure 3 shows the Raman spectra recorded for chemically reduced graphene nanosheets and cobalt oxide–graphene nanosheets composite. Raman spectrum of the reduced graphene contains the typical graphitic band at 1582  $cm^{-1}$  along with D band at 1355  $cm^{-1}$ . D band appears in the graphene due to the inelastic scattering of charge carriers by a phonon and then a second scattering by a defect or a zone boundary must occur to result in a recombination [31]. 2D band located at 2695  $cm^{-1}$ , originates from the second order overtone due to the secondary inelastic scattering from a second phonon [32]. Appearance of the G band confirms the reestablishment



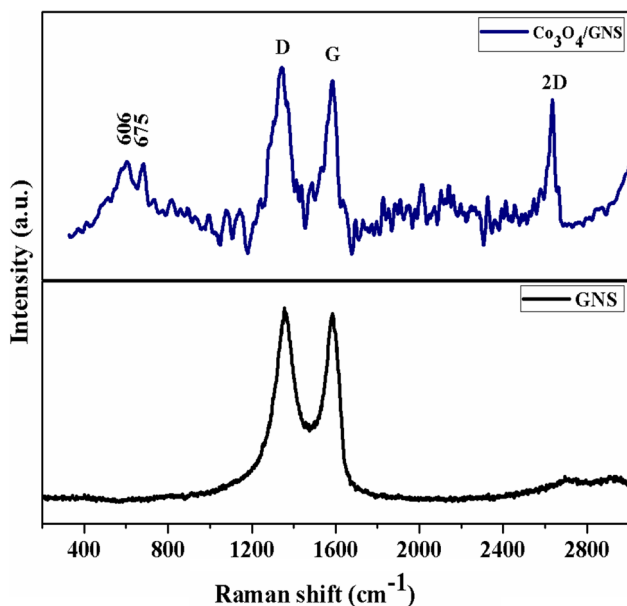


**Fig. 3** Raman spectra recorded for graphene nanosheet and graphene nanosheet—cobalt oxide composite material

of the conjugated graphene network of the  $sp^2$  bonded carbon atoms. Raman spectrum of composite material holds the signature peaks of graphene and cobalt oxide. Peaks found in the lower wavenumber region ( $400\text{--}700\text{ cm}^{-1}$ ) of the spectrum correspond to Co–O vibrations. Particularly, the peaks at  $606$  and  $675\text{ cm}^{-1}$  was assigned to the  $F_{2g}^2$  and  $A_g^1$  modes of crystalline  $Co_3O_4$ , respectively [33]. In the composite material, there was a small shift in the G band and an increase in the 2D band intensity. Generally, the integral ratio of peak intensities  $I_{2D}/I_G$  gives an estimate of number of layers in the stacked graphene. A small red shift experienced by G band along with increased intensity of 2D band indicates the increase in number of layers of graphene in the composite [34].

### 3.4 XPS studies

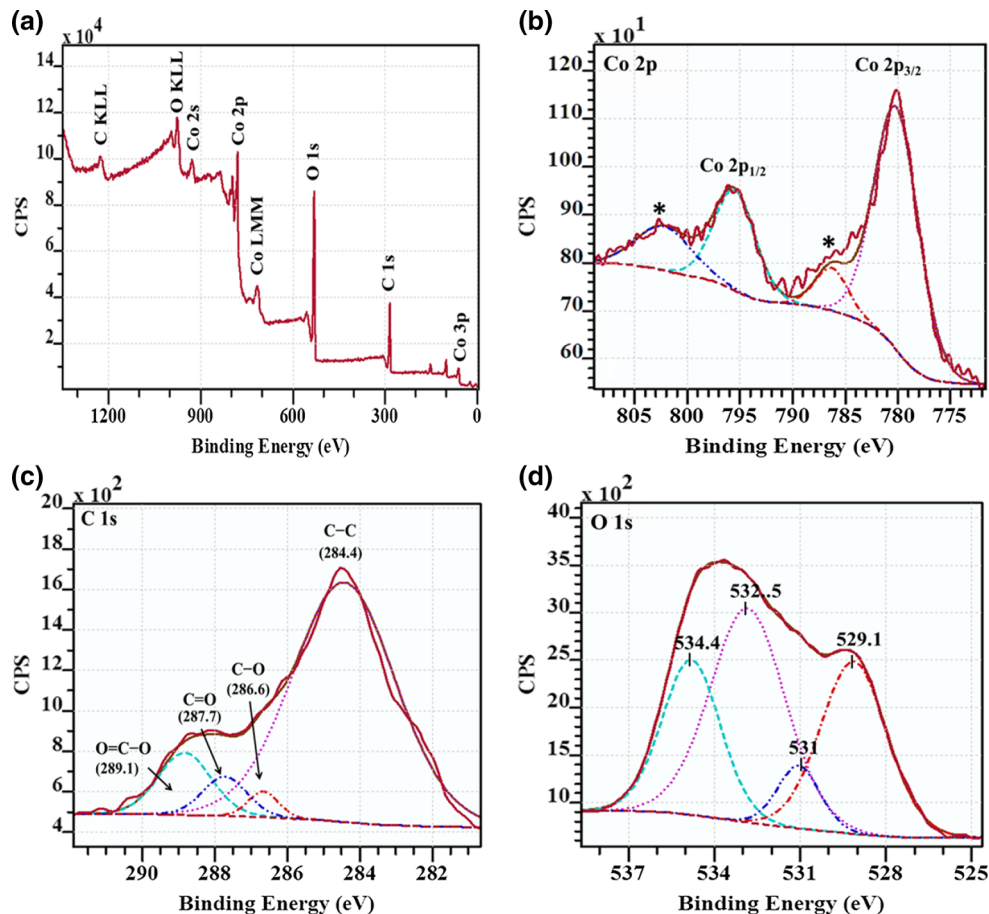
Chemical composition and chemical state of a material can be qualitatively and quantitatively analyzed using X-ray photoelectron spectroscopy (XPS). Figure 4a shows the surface composition analysis of the  $Co_3O_4$ –GNS composite sample that reveals the presence of Co, O and C elements. Purity of the prepared material can be justified from the survey spectrum. Detailed information on the elements oxidation state was obtained from the high resolution spectrum of Co 2p shown in Fig. 4b. Co 2p spectrum exhibits two major peaks of binding energy  $780.11$  and  $795.49\text{ eV}$  corresponding to Co  $2p_{3/2}$  and Co

$2p_{1/2}$  respectively, with a spin orbit splitting energy of  $15.38\text{ eV}$ . Additionally two shake up satellite peaks (marked by asterisk) characteristics of spinel phase of cobalt oxide ( $Co_3O_4$ ) were observed. Appearance of first satellite peak  $3.5\text{--}6.5\text{ eV}$  above the Co  $2p_{3/2}$  peak is the characteristics of  $Co^{2+}$  ions, and second satellite peak  $9\text{--}10\text{ eV}$  above the Co  $2p_{1/2}$  main peak is characteristic of  $Co^{3+}$  ions [35]. This further confirms the  $Co_3O_4$  spinel phase formation of cobalt oxide as determined from the XRD studies. Figure 4c shows the C 1s peak observed at  $284.4\text{ eV}$  which was deconvoluted into its four component peaks. Peaks at  $284.4$ ,  $286.6$ ,  $287.7$  and  $290.1\text{ eV}$  was attributed to the  $sp^2$  graphitic carbon (C–C), carbon present in alcohol, phenol or ether (C–O), carbonyl or quinone groups (C=O) and carboxyl groups (O=C–O) respectively [19]. Though oxygen containing functional groups was present in the reduced graphene, their intensities were relatively small compared to the graphitic  $sp^2$  carbon peak intensity. This once again confirms the sufficient reduction of GO to graphene. Further, O 1s peak was deconvoluted into four peaks (Fig. 4d), one about  $529.1\text{ eV}$  corresponds to metal oxygen bond (Co–O), second peak at  $531\text{ eV}$  is typical of oxygen in an OH group and strongly supports the presence of a hydroxyl species such as  $CoOOH$  and C–OH, third at  $532.5\text{ eV}$  corresponds to surface bonded water (H–O–H) and peak at  $534.4\text{ eV}$  was associated with C–O groups [26]. Results obtained from XPS studies corroborate well with the findings from FTIR studies.

### 3.5 Morphological studies

Surface morphology of the prepared samples was investigated using FESEM images. Figure 5a shows the high magnification image of chemically reduced crumbled graphene nanosheets. Independent sheets of graphene had combined to form flower like graphene nanosheet clusters. Figure 5b of the figure shows the agglomerated morphology of the pristine cobalt oxide. Thin nano-rod like structures can be seen here and there on the surface of cobalt oxide. Low and high magnification images of the composite material depict the porous morphology induced by the graphene sheets evident from Fig. 5c, d, respectively. High magnification images reveal sheet like nature of graphene being preserved in the composite material. Aggregates of cobalt oxide nanoparticles were found to form alongside of graphene nanosheets. Introduction of graphene has created diffusion channels for electrolyte ions to access the interior of the bulk electrode. These pores will reduce the diffusion length and aid rapid insertion/exertion of electrolyte ions.

**Fig. 4** **a** XPS survey spectrum of the composite material, **b** the high resolution XPS spectrum of Co 2p peak splitted into Co 2p<sub>1/2</sub> and Co 2p<sub>3/2</sub> peaks, **c** C 1s spectrum deconvoluted into component peaks and **d** O 1s spectrum of the composite material

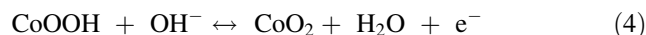
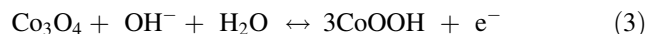


### 3.6 Electrochemical studies

#### 3.6.1 Cyclic voltammetry studies

Current versus voltage characteristics of the samples were obtained using cyclic voltammetry (CV) technique. CV curves recorded for Co<sub>3</sub>O<sub>4</sub> and GNS–Co<sub>3</sub>O<sub>4</sub> at 25 mV/s scan rate is displayed in Fig. 6. CV curves recorded at low scan rates depict the actual capacitive behaviour of the material. Pair of cathodic and anodic peaks appeared for pristine cobalt oxide converges to a pair of redox peaks for GNS–Co<sub>3</sub>O<sub>4</sub> composite. Graphene provides good electrical support to the composite; charge transfers within the composite were highly accelerated which can be understood from the merging of two pairs of redox peaks into single pair. Presence of redox peaks in the CV curves illustrates the charge storage mechanism as faradaic and the capacitive behaviour was pseudocapacitive. Contribution from electric double layer capacitance can be inferred from the near rectangular shape of the CV curve within the potential range of 0–0.2 V. It is to be noted that the electric double layer region in the CV curve of composite was increased substantially. Enhancement in the double layer

capacitance of the electrode material can be attributed to the electrochemical reactivity of graphene in the composite. Graphene also contributes to the electric double layer capacitance by facilitating ion transportation. Large current response of the electrode materials is associated with the faradaic region of the CV curve. Redox peaks exhibited by cobalt oxide can be ascribed to the reversible transition between two type of ions Co<sup>2+</sup> and Co<sup>3+</sup> present in the tetrahedral and octahedral sites of spinel oxide respectively (Co<sup>2+</sup> ↔ Co<sup>3+</sup> and Co<sup>3+</sup> ↔ Co<sup>4+</sup>) [27].



High current response observed for the graphene nanosheets-cobalt oxide composite can be related to the improved electrical conductivity provided by the graphene nanosheets. Clearly, CV curve of the GNS–Co<sub>3</sub>O<sub>4</sub> composite possess large integrated area compared to pure cobalt oxide. Larger area under the CV curve means higher specific capacitance. Diffusion channels created by graphene nanosheets incorporated within cobalt oxide

**Fig. 5** The FESEM images of the samples prepared **a** flower like graphene nanosheets (GNS), **b** agglomerated  $\text{Co}_3\text{O}_4$  nanoparticles, **c, d** low and high magnification images of the GNS– $\text{Co}_3\text{O}_4$  composite respectively

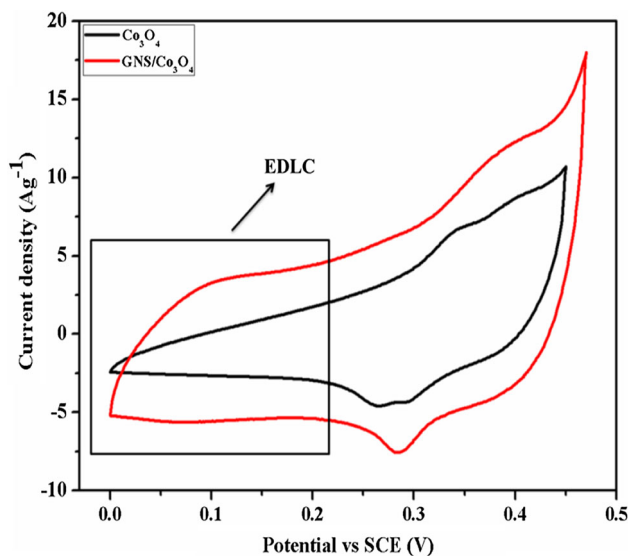
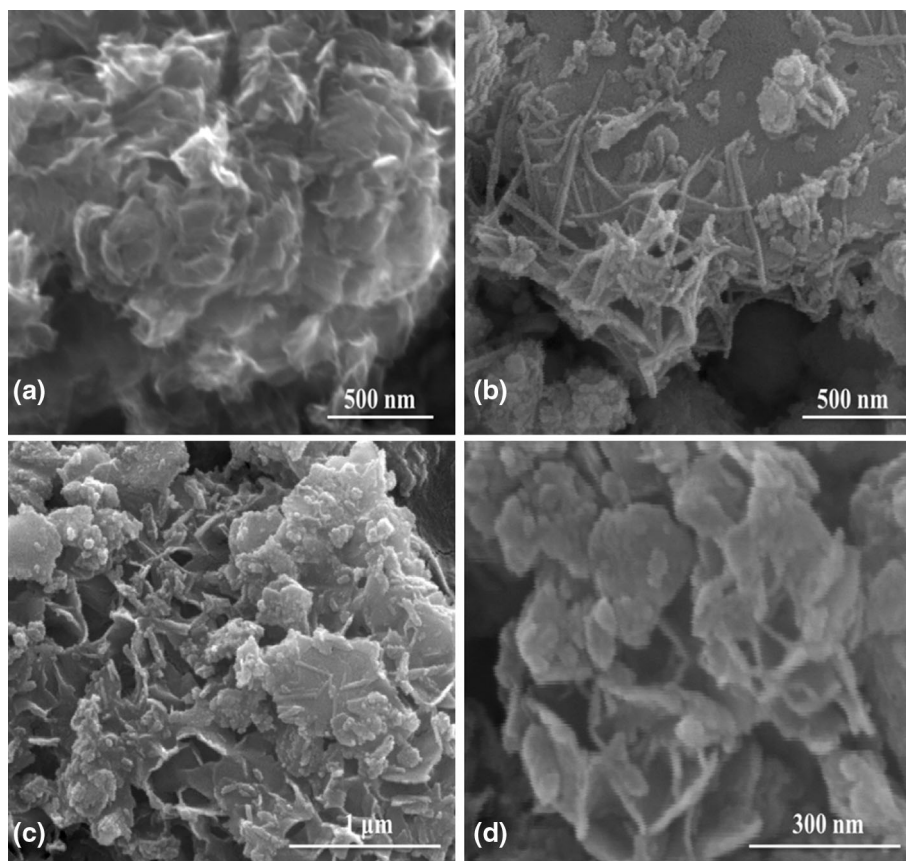


**Fig. 6** Cyclic voltammograms recorded for  $\text{Co}_3\text{O}_4$  and GNS– $\text{Co}_3\text{O}_4$  at 25 mV/s scan rate in 1 M KOH electrolyte using SCE as reference electrode

aggregates have facilitated rapid insertion/exertion of electrolyte ions at high scan rates resulted in increased specific capacitance. With the increase in sweep rate

current response increases, which were recorded and presented in Fig. 7a, b. With increase in scan rate CV shape of pristine cobalt oxide changes notably. At 100 mV, two pair of redox peaks observed at low scan rate converged to single redox pair. This is because at low scan rates electrolyte ions have sufficient time to diffuse into the electrode material and react with all available electro-active species but at high scan rates only surface active sites participate in the electrochemical reaction. In our case, the current density measured for anodic sweep and cathodic sweep were unequal, therefore these transitions were quasi reversible. Fast reversible transition in the electrode material was hindered by the diffusion controlled rate kinetics of the electrolyte ions. Figure 7c displays the Randles–Sevcik plot, anodic peak current density ( $i_{p, a}$ ) vs square root of scan rate ( $v^{1/2}$ ). Linear relationship between them indicates the diffusion controlled rate kinetics of the electrode process. As the scan rate increases anodic and cathodic peaks shift to the left and right respectively for pristine cobalt oxide due to the polarization resistance. But for graphene nanosheet-cobalt oxide composite the CV shape remains intact with increase in the scan rate portraying its electrochemical stability and high power capability. Specific capacitance of the electrode material can be calculated



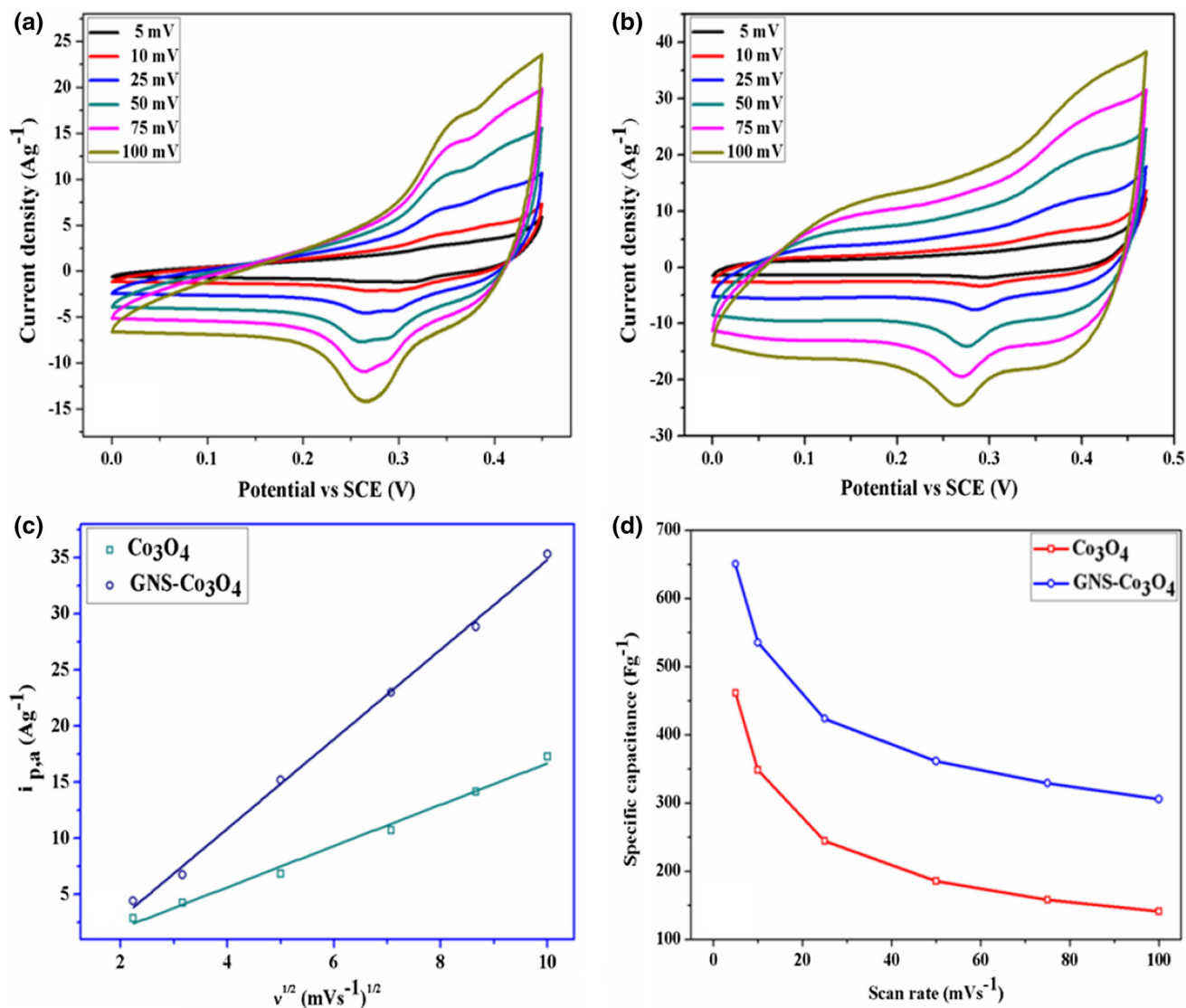


**Fig. 7** **a, b** The CV curves recorded at various scan rates (5–100 mV/s) for  $\text{Co}_3\text{O}_4$  and GNS- $\text{Co}_3\text{O}_4$  respectively, **c** Randles–Sevcik plot depicting the diffusion controlled process and **d** displays the graphical representation of specific capacitance calculated at various scan rates

from the CV study using below equation reported earlier [36]:

$$SC = \frac{1}{v \times m(V_a - V_c)} \int_{V_a}^{V_c} IVdV \quad (5)$$

The SC values were calculated graphically by integrating the area under the I–V curves and then dividing by the sweep rate  $v$  (V/s), the mass of the material ( $m$ ), and the potential window ( $V_a - V_c$ ). Among the prepared materials GNS- $\text{Co}_3\text{O}_4$  composite holds the maximum specific capacitance of 650 F/g at 5 mV scan rate while  $\text{Co}_3\text{O}_4$  shows only 461 F/g capacitance. Graphene addition has aided in circumventing the drawbacks faced by pristine cobalt oxide. Obtained specific capacitance is higher than

rGO/ $\text{Co}_3\text{O}_4$  composite (291 F/g at 1 A/g) prepared by homogeneous incorporation of reduced graphene oxide sheets in cobalt oxide matrix reported by Wang et al. [15], while Park et al. [39] prepared  $\text{Co}_3\text{O}_4$ -GNS exhibited 396 F/g at 5 mV/s scan rate, Zhou et al. [40] derived  $\text{Co}_3\text{O}_4$ -reduced graphene oxide scrolls demonstrated only 159.8 F/g at 5 mV/s scan rate and rapid microwave assisted synthesized graphene nanosheet/ $\text{Co}_3\text{O}_4$  composite prepared by J. Yan et al. shows 243.2 F/g at 10 mV/s in 6 M KOH electrolyte [41]. High capacitance was due to the synergistic combination of good electro-activeness of cobalt oxide and high electrical conductivity of graphene nanosheets. SC calculated at various scan rates were graphically represented in Fig. 7d.

3.6.2 Galvanostatic charge–discharge studies

Rate capability of the electrode material was further tested from galvanostatic charge–discharge study using chronopotentiometry (CP) technique. CP curve of the samples recorded at 1 A/g current density was displayed in Fig. 8a. Two kinds of variation in the curve were observed, a linear variation with time between 0–0.2 V was typical of electric double layer capacitance and sloped variation after that resembles pseudocapacitive behaviour [37]. Charging time was not completely identical to the discharge time for the prepared samples due to the mild irreversibility in the redox transitions. Results obtained from CP study well

coincide with CV study results. Figure 8b, c shows the CP curve of Co<sub>3</sub>O<sub>4</sub> and GNS–Co<sub>3</sub>O<sub>4</sub> recorded for different current densities. Specific capacitance of the samples can be calculated from the charge–discharge study using below equation [12]:

$$SC = \frac{I \times t_d}{m \times \Delta V} \tag{6}$$

I is the constant current applied, t<sub>d</sub> is the discharge time, m is the mass of the material loaded and ΔV is the potential difference. Specific capacitance calculated from CP study was tabulated in Table 1. Cycling life of the electrode is as important as any other parameters scrutinized for

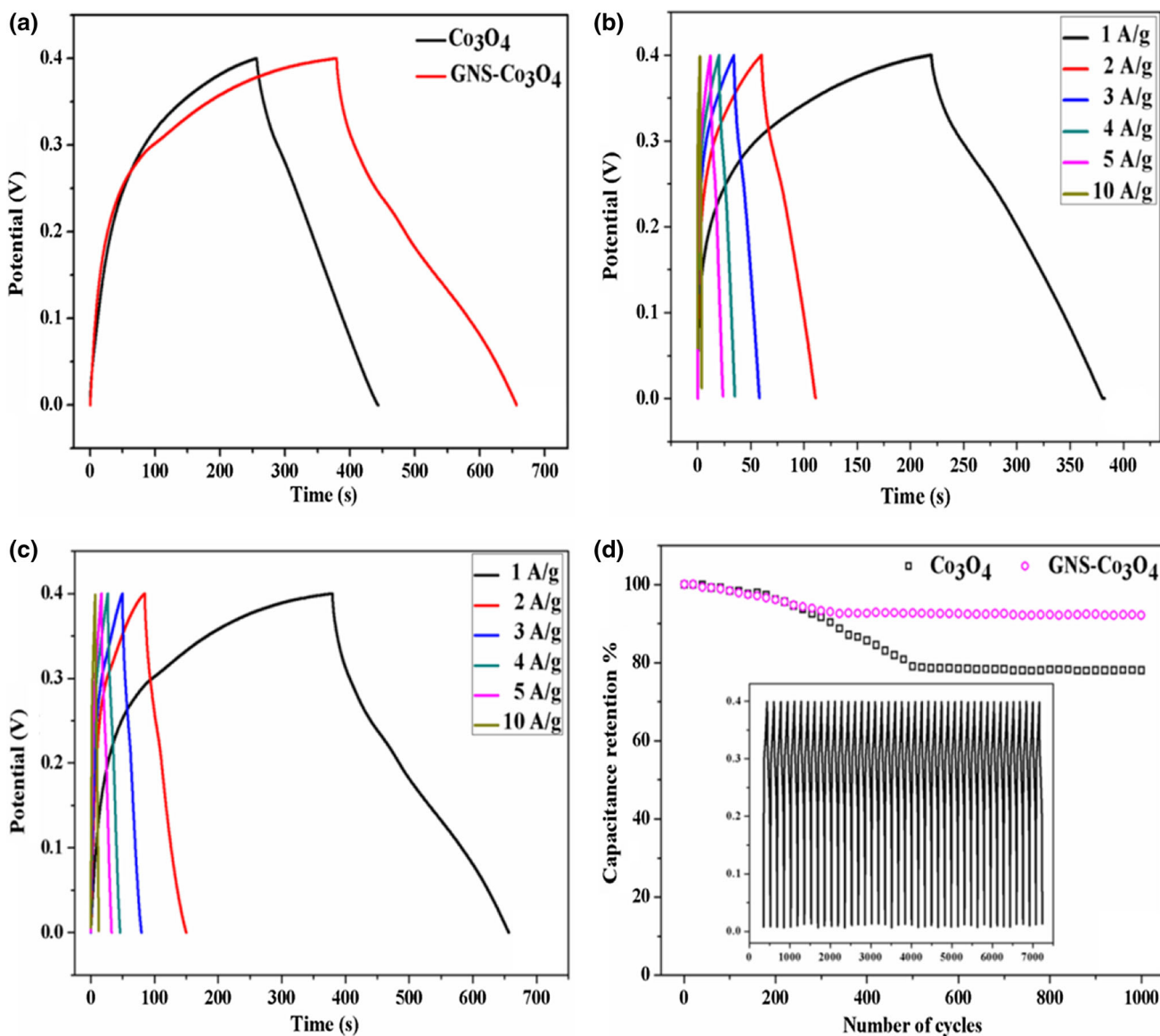


**Fig. 8** a Demonstrates the charge–discharge profiles of Co<sub>3</sub>O<sub>4</sub> and GNS–Co<sub>3</sub>O<sub>4</sub> recorded at 1 A/g current density in 1 M KOH electrolyte, b, c the charge–discharges curves recorded at various

current densities (1–10 A/g) for Co<sub>3</sub>O<sub>4</sub> and GNS–Co<sub>3</sub>O<sub>4</sub> respectively and d displays the results of long cycling measurement conducted for 1000 cycles

**Table 1** Specific capacitances of electrodes measured at various current densities in 1 M KOH

Current density (A/g)	Electrode specimens	
	Co <sub>3</sub> O <sub>4</sub> (F/g)	GNS–Co <sub>3</sub> O <sub>4</sub> (F/g)
1	405	641
2	250	340
3	187.5	262.5
4	150	230
5	150	212.5
10	75	175

supercapacitor application. Electrodes were subjected to continuous cycling for 1000 cycles at high current density of 3 A/g and the results were presented in Fig. 8d. 92 % of the original capacitance was retained by GNS–Co<sub>3</sub>O<sub>4</sub> composite at the end of 1000 cycles, which is higher compared to Co<sub>3</sub>O<sub>4</sub>–GNS prepared by Park et al. [42]. Graphene cobalt oxide composite exhibits better cycling stability over the pristine cobalt oxide. The excellent specific capacitance and cycle performance at high current density can be attributed to the following reasons. First, the graphene nanosheets have improved the electrical conductivity of the composite. Second, the porous morphology induced by the graphene sheets aid facile electrolyte ion transport to the bulk. Third, graphene acts as a buffer for the volume change during the charge–discharge process providing an assurance for improved cycling stability. Finally, the presence of GNS will contribute to the electric double layer which increases the facility of OH<sup>−</sup> transportation during the rapid charge–discharge process [38].

### 3.6.3 Electrochemical impedance studies

Electrochemical impedance spectroscopy (EIS) was also employed to characterize the samples. Figure 9 shows the complex impedance plot (Nyquist plot) between  $Z'$  and  $-Z''$  recorded between 1 Hz–100 kHz frequency region. Inset of the figure shows the enlarged portion of the high frequency region. Interception of the spectra on X-axis gives an estimate of the equivalent series resistance (ESR) or solution resistance ( $R_s$ ). Inset of the Fig. 9 shows the enlarged portion of the high frequency region. Clearly, GNS–Co<sub>3</sub>O<sub>4</sub> exhibits higher electrical conductivity or vice versa lower resistance than pristine cobalt oxide (Co<sub>3</sub>O<sub>4</sub>). This demonstrates the role of GNS in improving the conductivity of the composite leading to higher current response. ESR value of 1.9  $\Omega$  observed for GNS–Co<sub>3</sub>O<sub>4</sub> was much lower compared to 3.40  $\Omega$  observed for Co<sub>3</sub>O<sub>4</sub>. ESR is considered as the consolidation of contribution from (1) resistance due to discontinuity in charge transfer

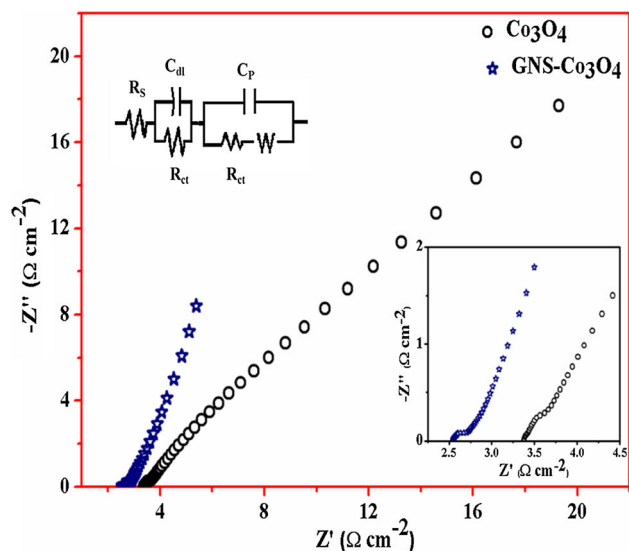


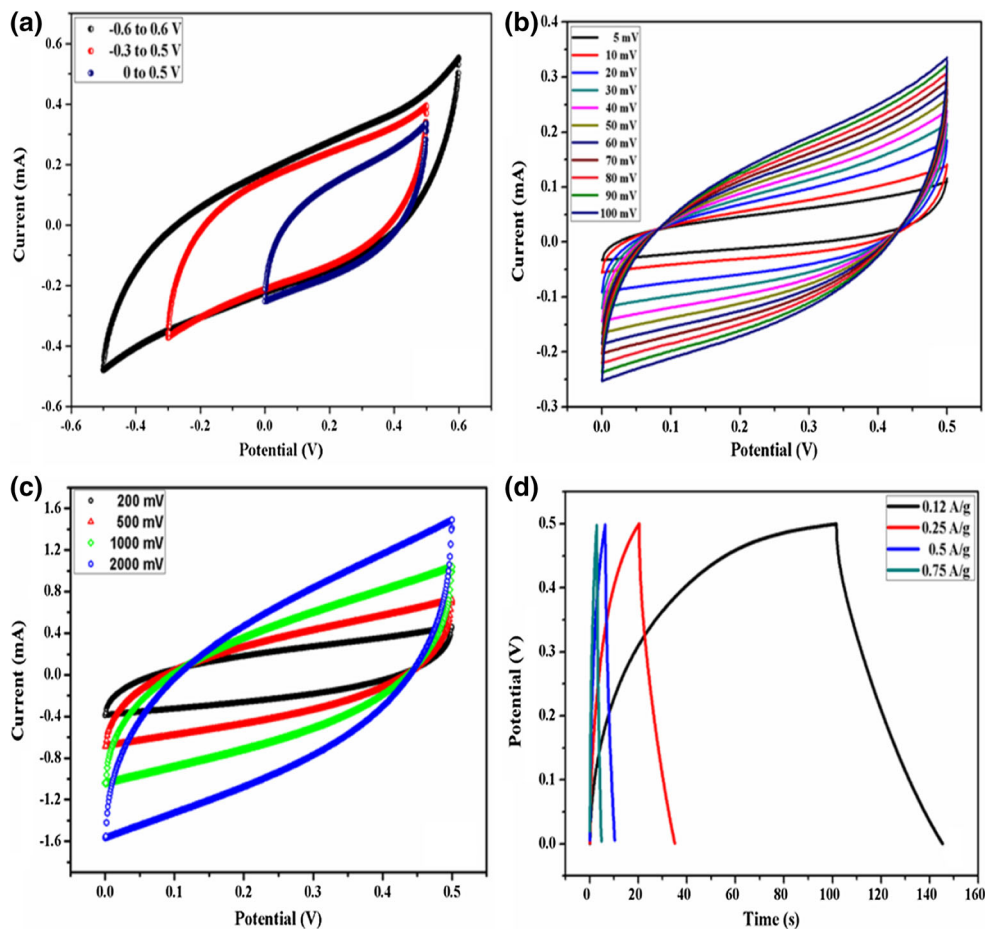
**Fig. 9** Complex plane impedance plot (Nyquist plot) recorded for the samples between 1 Hz and 100 kHz. Inset of the figure provides the magnified portion of high frequency region and Randle's equivalent circuit that best fits the spectra

process between solid oxide (electronic conductivity) and liquid electrolyte (ionic conductivity) (2) contact resistance between current collector and electrode material and (3) electrode materials intrinsic resistance [36]. An arc like incomplete semicircle was observed at the mid frequency region of the spectra, diameter of the semicircle is generally considered as the charge transfer resistance  $R_{ct}$  [27]. This depicts the small charge transfer resistance in the prepared materials. Straight line observed in the low frequency region is a characteristic of Warburg impedance or diffusion resistance. Slope of the line gives the measure of diffusion resistance offered by the materials. GNS–Co<sub>3</sub>O<sub>4</sub> composite offers low diffusion resistance for the electrolyte ions. Equivalent circuit that best fits the observed spectra is provided in the inset of Fig. 9, where  $C_{dl}$  is the double layer capacitance.

### 3.6.4 Symmetric two electrode cell assembly and electrochemical characterization

To test the actual performance of the prepared electrode material in the real capacitor condition, a two electrode cell assembly was fabricated using GNS–Co<sub>3</sub>O<sub>4</sub>. Symmetrical capacitor fabricated was subjected to electrochemical characterizations and the results were presented in Fig. 10. CV curves recorded for three different potential window in 3 M KOH electrolyte at 100 mV/s scan rate is shown in Fig. 10a. Deviation in the shape of CV curve from ideal rectangular shape indicates the pseudocapacitive nature of the charge storage. Beyond 0.6 V a steep current increase

**Fig. 10** Presents the electrochemical results of fabricated GNS–Co<sub>3</sub>O<sub>4</sub> symmetrical cell **a** the CV curve recorded at 100 mV/s scan rate for three different potential window, **b** the CV curves recorded from 5 to 100 mV/s scan rate, **c** the CV curves recorded at very high scan rates and **d** displays the charge–discharge curve recorded for various current densities



was noticed in the highest-voltage range, which is related to the dioxygen evolution at the electrodes [43]. Figure 10b shows the CV curves recorded from 5–100 mV/s scan rate. CV curves were found to be symmetrical at high scan rate compared to low scan rates. Current density increases linearly with the increase in scan rate without any change in the CV shape which illustrates the high rate capability of the material. Superior ultrafast response of the electrode material was demonstrated by conducting the CV measurements at very high scan rates of 200, 500, 1000 and 2000 mV/s, as shown in Fig. 10c. Fabricated symmetrical supercapacitor was able to retain its original shape and symmetry at very high scan rates. Ultra-fast response can be attributed to the superior electrical conductivity and electron transport speedway created by graphene nanosheets in the composite. Specific capacitance ( $C_{SC}$ ) of the cell was calculated using the below equation [44]

$$C_{SC} = \frac{4 \times C}{m}$$

$C$  capacitance of the cell experimentally calculated,  $m$  total mass of the electrodes. Fabricated symmetric capacitor exhibited a high capacitance of 104 F/g at 5 mV/s scan rate. Charge–discharge curves recorded at various current

densities were presented in Fig. 10d. CP results well match the findings of CV studies. Hence, GNS–Co<sub>3</sub>O<sub>4</sub> based symmetrical supercapacitors are most desirable for high power applications.

## 4 Conclusion

A simple room temperature method has been developed to prepare exfoliated graphene oxide at low temperature (150 °C) and subsequently reduced to graphene nanosheets via chemical reduction method. Cobalt oxide/graphene nanosheet composite was prepared to evaluate the impact of graphene on the electrochemical performance of the composite material. Successful compound formation was confirmed and structural details were obtained from XRD studies. FTIR studies provide insight on the functional groups attached to the prepared materials. XPS measurement confirms the composite formation and removal of oxygen containing functional groups in the reduced graphene. Significant influence of graphene on the compound morphology was investigated using FESEM images. In the composite material, cobalt oxide particle aggregation



decreases with the introduction of graphene nanosheets. Better specific capacitance of the composite material over pristine cobalt oxide was inferred from their respective CV curves. Pseudocapacitive behaviour of the electrode was once again identified from the charge–discharge study. Composite material exhibits better cycling integrity compared to pristine cobalt oxide. Graphene nanosheets have improved the electrical conductivity of the  $\text{Co}_3\text{O}_4$ –GNS composite, cognizant from the EIS measurements. Symmetrical supercapacitor fabricated using GNS– $\text{Co}_3\text{O}_4$  demonstrates superior rate kinetics. This synergistic combination of  $\text{Co}_3\text{O}_4$  and GNS is a promising candidate for high power supercapacitor applications.

**Acknowledgments** Financial support from Anna University by providing Anna Centenary Research Fellowship (ACRF) for A. Nirmallesh Naveen is highly appreciated (Lr. No. CR/ACRF/2013/37).

## References

- X.H. Xia, J.P. Tu, Y. Zhang, Y.J. Mai, X.L. Wang, C.D. Gu, X.B. Zhao, *RSC Adv.* **2**, 1835–1841 (2012)
- H. Jiu, C. Huang, L. Zhang, J. Chang, H. Jiao, S. Zhang, W.B. Jia, *J. Mater. Sci. Mater. Electron.* (2015). doi:10.1007/s10854-015-3505-2
- M.S. Song, K.M. Lee, Y.R. Lee, I.Y. Kim, T.W. Kim, J.L. Gunjaker, S.J. Hwang, *J. Phys. Chem. C* **114**, 22134–22140 (2010)
- R.R. Salunkhe, K. Jang, S.W. Lee, H. Ahn, *RSC Adv.* **2**, 3190–3193 (2012)
- L. Hou, C. Yuan, L. Yang, L. Shen, F. Zhang, X. Zhang, *RSC Adv.* **1**, 1521–1526 (2011)
- R. Ding, L. Qi, H. Wang, *J. Solid State Electrochem.* **16**, 3621–3633 (2012)
- J. Zhi, S. Deng, Y. Zhang, Y. Wang, A. Hu, *J. Mater. Chem. A* **1**, 3171–3176 (2013)
- D. Han, P. Xu, X. Jing, J. Wang, D. Song, J. Liu, M. Zhang, *J. Solid State Chem* **203**, 60–67 (2013)
- J. Zhang, D. Shu, T. Zhang, H. Chen, H. Zhao, Y. Wang, Z. Sun, S. Tang, X. Fang, X. Cao, *J. Alloys Compd.* **532**, 1–9 (2012)
- Y.I. Yoon, J.M. Ko, CoNi oxide/carbon-nanofiber composite electrodes for supercapacitors. *Int. J. Electrochem. Sci.* **3**, 1340–1347 (2008)
- B. Babakhani, D.G. Ivey, *Electrochim. Acta* **56**, 4753–4762 (2011)
- A.N. Naveen, S. Selladurai, *AIP Conf. Proc.* **1591**, 246–248 (2014)
- J.M. Luo, B. Gao, X.G. Zhang, *Mater. Res. Bull.* **43**, 1119–1125 (2008)
- H.Y. Wu, H.W. Wang, *Int. J. Electrochem. Sci.* **7**, 4405–4417 (2012)
- H.W. Wang, Z.A. Hu, Y.Q. Chang, Y.L. Chen, Z.Y. Zhang, Y.Y. Yang, H.Y. Wu, *Mater. Chem. Phys.* **130**, 672–679 (2011)
- D. Chen, L. Tang, J. Li, *Chem. Soc. Rev.* **39**, 3157–3180 (2010)
- V. Thirumal, A. Pandurangan, R. Jayavel, K.S. Venkatesh, N.S. Palani, R. Ragavan, R. Ilangovan, *J. Mater. Sci. Mater. Electron.* **26**, 6319–6328 (2015)
- M. Jin, H.K. Jeong, T.H. Kim, K.P. So, Y. Cui, W.J. Yu, E.J. Ra, Y.H. Lee, *J. Phys. D Appl. Phys.* **43**, 275402 (2010)
- S. Stankovich, D.A. Dikin, R.D. Piner, K.A. Kohlhaas, A. Kleinhammes, Y. Jia, Y. Wu, S.T. Nguyen, R.S. Ruoff, *Carbon* **45**, 1558–1565 (2007)
- Y. Zhu, S. Murali, M.D. Stoller, A. Velamakanni, R.D. Piner, R.S. Ruoff, *Carbon* **48**, 2106–2122 (2010)
- C. Zhang, W. Lv, X. Xie, D. Tang, C. Liu, Q.H. Yang, *Carbon* **6**, 211–224 (2013)
- S. Kaniyoor, T.T. Baby, S. Ramaprabhu, *J. Mater. Chem.* **20**, 8467–8469 (2010)
- Z. Ji, G. Zhu, X. Shen, H. Zhou, C. Wu, M. Wang, *N. J. Chem.* **36**, 1774–1780 (2012)
- C.M. Willemse, K. Thhomelang, N. Jahed, P.G. Baker, E.I. Iwuoha, *Sensors* **11**, 3970–3987 (2011)
- D.C. Marcano, D.V. Kosynkin, J.M. Berlin, A. Sinititskii, Z. Sun, A. Slesarev, L.B. Alemany, W. Lu, J.M. Tour, *ACS Nano* **4**(8), 4806–4814 (2010)
- A.N. Naveen, S. Selladurai, *Electrochim. Acta* **125**, 404–414 (2014)
- S.K. Meher, G.R. Rao, *J. Phys. Chem. C* **115**, 25543–25556 (2011)
- L. Xie, K. Li, G. Sun, Z. Hu, Z. Lv, J. Wang, C. Zhang, *J. Solid State Electrochem.* **17**, 55–61 (2013)
- L. Ren, K.S. Hui, K.N. Hui, *J. Mater. Chem. A* **1**, 5689–5694 (2013)
- W. Chen, L. Yan, *Nanoscale* **2**, 559–563 (2010)
- C. Thomsen, S. Reich, *Phys. Rev. Lett.* **85**(24), 5214–5217 (2000)
- R. Narula, S. Reich, *Phys. Rev. B* **78**, 165422 (2–6) (2008)
- X.C. Dong, H. Xu, X.W. Wang, Y.X. Huang, M.B. Chan-Park, H. Zhang, L.H. Wang, W. Huang, P. Chen, *ACS Nano* **6**(4), 3206–3213 (2012)
- A.C. Ferrari, *Solid State Commun.* **143**, 47–57 (2007)
- J.L. Gautier, E. Rios, M. Gracia, J.F. Marco, J.R. Gancedo, *Thin Solid Films* **311**, 51–57 (1997)
- S.K. Meher, G.R. Rao, *J. Phys. Chem. C* **115**, 15646–15654 (2011)
- F. Zhang, L. Hao, L. Zhang, X. Zhang, *Int. J. Electrochem. Sci.* **6**, 2943–2954 (2011)
- B. Zhao, J. Song, P. Liu, W. Xu, T. Fang, Z. Jiao, H. Zhang, Y. Jiang, *J. Mater. Chem.* **21**, 18792–18798 (2011)
- S. Park, S.J. Park, S. Kim, *Carbon Lett.* **13**(2), 130–132 (2012)
- W. Zhou, J. Liu, T. Chen, K.S. Tan, X. Jia, Z. Luo, C. Cong, H. Yang, C.M. Li, T. Yu, *Phys. Chem. Chem. Phys.* **13**, 14462–14465 (2011)
- J. Yan, T. Wei, W. Qiao, B. Shao, Q. Zhao, L. Zhang, Z. Fan, *Electrochim. Acta* **55**, 6973–6978 (2010)
- S. Park, S.J. Park, S. Kim, *Bull. Korean Chem. Soc.* **33**(12), 4247–4250 (2012)
- V. Khomenko, E.R. Pinero, E. Frackowiak, F. Béguin, *Appl. Phys. A* **82**, 567–573 (2006)
- A.N. Naveen, S. Selladurai, *Electrochim. Acta* **173**, 290–301 (2015)